

# Variational Destriping in Remote Sensing Imagery: Total Variation with $L^1$ Fidelity

Konstantin Dragomiretskiy and Igor Yanovsky

## Abstract

This paper introduces a variational method for destriping data acquired by pushbroom-type satellite imaging systems. The model leverages sparsity in signals and is based on current research in sparse optimization and compressed sensing. It is based on the basic principles of regularization and data fidelity with certain constraints using modern methods in variational optimization - namely total variation (TV), both  $L^1$  and  $L^2$  fidelity, and the alternating direction method of multipliers (ADMM). The main algorithm in this paper, TV- $L^1$ , uses sparsity promoting energy functionals to achieve two important imaging effects. The TV term maintains boundary sharpness of content in the underlying clean image, while the  $L^1$  fidelity allows for the equitable removal of stripes without over- or under-penalization, providing a more accurate model of presumably independent sensors with unspecified and unrestricted bias distribution. A comparison is made between the TV- $L^1$  and TV- $L^2$  models to exemplify the qualitative efficacy of an  $L^1$  striping penalty. The model makes use of novel minimization splittings and proximal mapping operators, successfully yielding more realistic destriped images in very few iterations.

## Index Terms

Alternating direction method of multipliers (ADMM), compressed sensing, image striping restoration, raster scan, sparse optimization, split Bregman, total variation, variational destriping

This work was supported by the National Science Foundation under Grant DMS 1217239 and the W. M. Keck Foundation. The research was carried out in part at the Jet Propulsion Laboratory, California Institute of Technology, under a contract with the National Aeronautics and Space Administration.

K. Dragomiretskiy is with the Department of Mathematics, University of California, Los Angeles (UCLA), Los Angeles, CA 90095 USA (e-mail: konstantin@math.ucla.edu)

I. Yanovsky is with the Jet Propulsion Laboratory, California Institute of Technology, Pasadena, CA 91109, USA and also with the Joint Institute for Regional Earth System Science and Engineering, University of California, Los Angeles, CA 90095 USA (e-mail: igor.yanovsky@jpl.nasa.gov)

© 2017. All rights reserved.

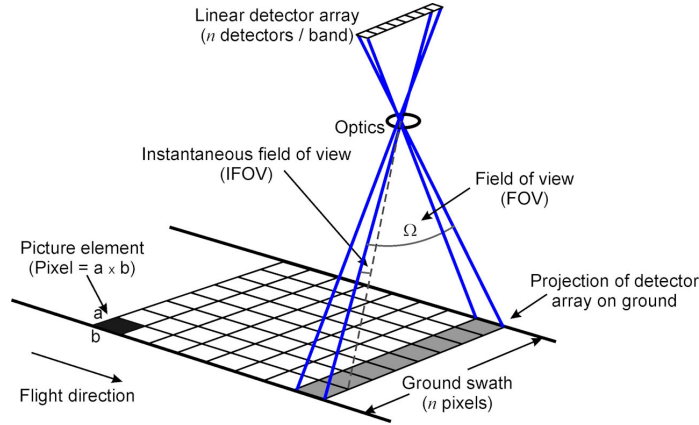


Fig. 1: Pushbroom Satellite Diagram

## I. INTRODUCTION

Image striping is a well-known phenomenon that arises in multi-detector imaging systems ranging from pushbroom-type instruments, such as the Airborne Multi-angle Spectro Polarimetric Imager (AirMSPI), to atomic force microscopy (AFM). Biases in lateral detection occur due to response variation in spatial detectors, such as in satellite imaging systems, or temporal changes, such as in raster scans. Though these systems are optimally pre-calibrated, post-processing, such as destriping, of data is prerequisite for accurate and valid analyses. Striping removal has been traditionally performed using either statistically based methods, [1], [2], or low-pass filtering in the frequency domain [3], [4], [5], [6], [7]. This method, however, does not remove stripes completely and has an effect of blurring the image. More recently, wavelet-based filtering methods have been proposed [8], [9], [10]. However, such methods also blur the images and produce ringing effects in reconstruction.

We follow the pedigree of variational and PDE-based methods applied to images [11], [12] in order to construct a well-defined, optimizable model yielding fast and quality destriping. During our research, we have come across a similar work achieved by a total variation and framelet regularization model [13]. The same authors proposed an anisotropic spectral-spatial total variation regularization to enhance the smoothness of solution along both the spectral and spatial dimension in [14]. Our model and results were found independently, but share a similar foundation. The focus of our paper is not about creating a sparse wavelet representation of the destriped image, but rather on how to remove the optimal striping mask while preserving high image fidelity. We include detailed derivations and a motivated evolution of the optimization problem with pedagogy in mind so that these novel variational methods can be accessible to all academic disciplines involved with image processing.

Our research is robust to both isotropic and anisotropic versions of total variation, whereas [13] argue that the anisotropic case is the only appropriate one. While it is true that the anisotropic case uses a decoupled energy for measure of smoothness and is therefore easier to minimize, isotropic total variation is not selective in which

direction smoothness is penalized. Image content smoothness (or lack thereof) is not known *a priori*, thus no preference should be immediately given to certain directions for evaluating smoothness.

In [13] and [14], the authors employed the  $L^2$  norm as the fidelity term. Our research considers both  $L^2$  and  $L^1$  penalties for striping size, and compares the two, ultimately favoring the  $L^1$  due to a wider yet tighter distribution of the striping mask. Using the  $L^1$  penalty, and depending on the data, the isotropic total variation, which theoretically uses more local information, allows for a qualitatively better, less invasive and more intelligent destriping.

We construct a variational model that is well-defined, qualitatively motivated, and easily minimized. The constructed energy uses sparsity promoting energy functionals, based on total variation and  $L^1$  energy, to achieve minimally invasive destriping. Both isotropic and anisotropic total variation, along with  $L^1$  and  $L^2$  energies, are considered in our variational model. The alternating direction method of multipliers (ADMM) (split-Bregman) is used in conjunction with non-linear proximal operators to efficiently optimize the energy, yielding quick and quality results.

## II. MODEL

### A. Striping structure

Let  $U(x, y)$  be a stripe-free image of size  $R$  by  $C$ , and let  $G(y)$  be a multiplicative stripe noise of length  $R$ . Then the observed image,  $F$  can be written as  $F(x, y) = G(x, y)U(x, y)$ . Taking logarithms yields an additive structure, more suitable for energy minimization methods. The model can now be written as  $f(x, y) = g(y) + u(x, y)$  where  $f(x, y) = \ln(F(x, y))$ ,  $g(x, y) = \ln(G(x, y))$ , and  $u(x, y) = \ln(U(x, y))$ .

Striping in images can be viewed as a structured noise, of which variations are mainly concentrated along one axis. This can be mathematically encoded as  $\|\nabla_x G\| \ll \|\nabla_y G\|$ , or with the logarithmic terms,  $\|\nabla_x g\| \ll \|\nabla_y g\|$ .

### B. Tikhonov minimization

A classical Tikhonov minimization problem would consist of a smoothness regularizer and a data fidelity term, both easily differentiable, with the striping constraint [15]:

$$\begin{aligned} \min_u \left\{ \|\nabla u(x, y)\|_2^2 + \frac{\lambda}{2} \|u(x, y) - f(x, y)\|_2^2 \right\} \\ \text{s.t. } \|\nabla_x g\| \ll \|\nabla_y g\| \end{aligned}$$

This constraint can be simplified by the approximation that  $\nabla_x G(x, y) = 0 \quad \forall(x, y)$ , which would make  $G(x, y) = G(y)$ , and  $g(x, y) = g(y)$ , functions of only one variable. Using the additive identity between  $f$ ,  $g$ , and  $u$  along with the constraint approximation, the new unconstrained minimization problem is:

$$\min_g \left\{ \|\nabla_y(f(x, y) - g(x, y))\|_2^2 + \frac{\lambda}{2} \|g(x, y)\|_2^2 \right\}$$

By taking the first variation of the energy and setting it to zero, closed form solution to this minimization problem is

$$\begin{aligned} g(x, y) &= (\nabla_y \cdot \nabla_y + \lambda I)^{-1} (\nabla_y \cdot \nabla_y f(x, y)) \\ &= \left( \frac{\partial^2}{\partial y^2} + \lambda I \right)^{-1} (f_{yy}(x, y)) \end{aligned}$$

However, this solution would cause  $g$  to become bivariate, in contradiction to the constraint. Instead, using the Cartesian regularity of our rectangular domain  $\Omega = I_x \times I_y$  and using  $g(x, y) = g(y)$ , we can come to a solution that is in agreement with the constraint by integrating with respect to  $x$ :

$$\int_{\Omega} g(x, y) dx = \int_{I_x} g(y) dx = g(y) \int_{I_x} dx = g(y) \mu(I_x) = \int_{I_x} \left( \frac{\partial^2}{\partial y^2} + \lambda I \right)^{-1} (f_{yy}(x, y)) dx \quad \Rightarrow$$

$$g(y) = \frac{1}{\mu(I_x)} \int_{I_x} \left( \frac{\partial^2}{\partial y^2} + \lambda I \right)^{-1} (f_{yy}(x, y)) dx$$

### C. Fourier interpretation

Utilizing the Plancherel Fourier isometry, the solution can be interpreted in spectral form as:

$$\hat{g}(\omega_y) = \frac{1}{\mu(I_x)} \left( \frac{\omega_y^2}{\lambda + \omega_y^2} \right) \hat{f} = \left( \frac{\omega_y^2}{\lambda + \omega_y^2} \right) \hat{f}$$

For a specific  $x$ , the stripping  $g(y)$  is constant of higher frequency, whereas the underlying clean image varies more slowly (has more low-frequency content) and while for each  $x$  having a somewhat different frequencies. Therefore, the average frequencies of the clean image are low in magnitude and of lower-frequency, while the average frequencies of the stripping are high in magnitude and of higher-frequency. Therefore, the average frequencies (averaged over  $\omega_x$ ) of the cleaned image are simply the average frequencies of the original image multiplied by a one dimensional Low-Pass filter  $\frac{\lambda}{\lambda + z^2}$ . Likewise, the stripping mask on the spectral side,  $\hat{g}$ , is obtained analogously with a one dimensional High-Pass filter  $\frac{z^2}{\lambda + z^2}$ .

Though this minimization problem is readily solvable in closed form and has a motivated physical interpretation, we must abandon the quadratic energy terms so that we may have less penalization for heavier striping and to allow for less smooth solutions. Though the differentiability of terms is nice, enough optimization machinery has been

developed that we may tread forward. We now investigate and outline some tools from signal processing in order to refine our model. Stripe and ring artifact removal from this frequency perspective has been accomplished using wavelet and Fourier filtering [16].

### III. TOOLS FROM FUNCTIONAL ANALYSIS

#### A. Total Variation: Anisotropic vs. Isotropic

The idea of using total variation as a regularizer and denoiser that promotes sparsity and piecewise constant smoothness dates back to Rudin, Osher, and Fatemi [17], [18]. We begin with defining the notion of total variation, which will be used as a regularizer in the model.

**Definition** The *total variation* of a function  $f \in L^1(\Omega)$  is

$$V(f, \Omega) := \sup \left\{ \int_{\Omega} f(x) \operatorname{div} \phi(x) \, dx : \phi \in C_c^1(\Omega, \mathbb{R}^n), \|\phi\|_{L^\infty(\Omega)} \leq 1 \right\}$$

For a differentiable function  $f \in \Omega$ , with  $\Omega \subseteq \mathbb{R}^n$ , the total variation of  $f$  can be written as

$$V(f, \Omega) = \int_{\Omega} |\nabla f(x)| \, dx$$

The choice of vectorial norm inside the integral yields two different types of total variation.

**Definition** *Isotropic* total variation:  $|\cdot|$  denotes the  $l_2$ -norm, in which case

$$V(f, \Omega) = \int_{\Omega} \left( \sum_i^n f_{x_i}^2(x) \right)^{\frac{1}{2}} \, dx$$

**Definition** *Anisotropic* total variation:  $|\cdot|$  denotes the  $l_1$ -norm, in which case

$$V(f, \Omega) = \int_{\Omega} \sum_i^n |f_{x_i}(x)| \, dx$$

The isotropic and anisotropic cases differ in terms of the geometries they each preserve. While the decoupled anisotropic total variation preserves piecewise constant orthogonal structures such as rectangular roofs, the coupled isotropic total variation preserves piecewise constant radial structures such as silos. Our model will be robust with respect to either choice of total variation and dual derivations of variable updates will be shown, however the experiments and results are based on the anisotropic definition.

### B. Shrinkage Proximal Operator

We will introduce a splitting variable and quadratic penalty into the model. The solution to the  $l_1$ -regularized least squares problem

$$\arg \min_{\vec{x}} \mu \|\vec{x}\|_1 + \frac{1}{2} \|\vec{x} - \vec{y}\|_2^2$$

is given by the soft threshold proximal mapping operator, shrinkage [19], [20]:

#### Definition

$$\text{Shrink}(\vec{x}, \mu) = S_\mu(\vec{x}) = \frac{\vec{x}}{|\vec{x}|} \max\{|\vec{x}| - \mu, 0\}$$

If  $\|\vec{x}\|_1 = \|x_1\| + \|x_2\|$ , as in the anisotropic case of total variation, the shrinkage is decoupled and done component wise. On the other hand, if  $\|\vec{x}\|_1 = \sqrt{\|x_1\|^2 + \|x_2\|^2}$ , as in the isotropic case, the terms are coupled and both components are updated simultaneously. Both variants have their merits, while the former is computationally simpler, the latter has the advantage of using more local information and may be more conformant to certain image processing application.

## IV. TV- $L^1$ ADMM MODEL

We will now make some technical modifications to our model, while preserving the qualitative ideas and motivations. The two energy components of the minimization problem are the smoothness regularizer and the data fidelity term. The energy of the data fidelity term,  $\frac{\lambda}{2} \|f(x, y) - u(x, y)\|_2^2 = \frac{\lambda}{2} \|g(y)\|_2^2$ , can be interpreted as the size of the striping mask. The  $L_2$  fidelity overly penalizes stripes of large magnitude, and likewise under-exaggerates the significance of stripes of small magnitude. In areas of no striping, we intend our (logarithm of the) striping mask to be very close to zero, while in areas of heavy striping, we wish to remove said striping and thus will yield a larger magnitude of our striping mask in that region. Using the  $L^1$  fidelity gives us a smaller striping mask in areas of no striping, leaving enough energy to remove the heavier striping in localized areas of the image. Because there is no prior knowledge of the distribution of the stripes, and qualitatively we may wish to remove deep striping effects while preserving sharp geometry, we believe it is better to update the model with an  $L_1$  striping penalty,  $\|g\|_1$ .

An  $L^2$  gradient term would cause over-smoothing of the retrieved clean image  $u(x, y)$ . This could cause a loss in boundary sharpness of elements in the image (e.g. lakes, rooftops, etc.), which seems important in the pursuit and usage of destriped images. Implementing a total variation based regularizer would act similarly to the  $L^2$  gradient but maintains boundary sharpness more natural to the underlying image. Though these terms are not differentiable, impeding a closed form solution, state-of-the-art nonlinear optimization algorithms are available for fast convergence to qualitatively meaningful minimizers. The unconstrained total variation  $L^1$  model (TV- $L^1$ ) is:

$$\min_u \left\{ V(u(x, y), I_x \times I_y) + \lambda \|u(x, y) - f(x, y)\|_1 \right\}$$

or equivalently, minimizing with respect to the striping mask  $g$ :

$$\min_g \left\{ V(f(x, y) - g(y), I_x \times I_y) + \lambda \|g(y)\|_1 \right\}$$

### A. Discretization

For the purpose of application and computation, we shall now move the problem into a discrete setting. Let  $\Omega = \{x_1, \dots, x_C\} \times \{y_1, \dots, y_R\}$  be an  $R \times C$  matrix. First variations will be approximated via forward differences, so that  $\frac{\partial f}{\partial y}(x_i, y_j) \approx f(x_i, y_{j+1}) - f(x_i, y_j) := \delta_y f_{i,j}$  for  $j = 1, \dots, R-1$  and analogously for  $\frac{\partial f}{\partial x} \approx f(x_{i+1}, y_j) - f(x_i, y_j) := \delta_x f_{i,j}$  for  $i = 1, \dots, C-1$ . We will take Neumann boundary conditions, so that on the forward boundary ( $i = C$  or  $j = R$ ), the derivative is set to zero.

$$D = \begin{bmatrix} -1 & 1 & 0 & \cdots & 0 & 0 \\ 0 & -1 & 1 & \cdots & 0 & 0 \\ \vdots & \vdots & \vdots & \ddots & \vdots & \vdots \\ 0 & 0 & 0 & \cdots & -1 & 1 \\ 0 & 0 & 0 & \cdots & 0 & 0 \end{bmatrix} \in M_{R \times R}(\mathbb{R})$$

$$\text{so that } Du(x_{i_0}, y) = (\delta_y u_{i_0,1}, \dots, \delta_y u_{i_0,R-1}, 0)^T$$

Isotropic total variation:

$$|\nabla^I f(x_i, y_j)| \approx \sqrt{(\delta_x f_{i,j})^2 + (\delta_y f_{i,j})^2}$$

Anisotropic total variation:

$$|\nabla^{AI} f(x_i, y_j)| \approx |\delta_x f_{i,j}| + |\delta_y f_{i,j}|$$

With these discrete operators defined, the discrete unconstrained TV- $L^1$  minimization problem is:

$$\min_g \left\{ \sum_{i,j} \|\langle \delta_x f_{i,j}, \delta_y (f_{i,j} - g_j) \rangle\|_1 + \lambda \|g(y)\|_1 \right\}$$

The two flavors of the minimization problem are:

Anisotropic

$$\min_g \left\{ \sum_{i,j} |\delta_y(f_{i,j} - g_j)| + \lambda \|g(y)\|_1 \right\}$$

Isotropic

$$\min_g \left\{ \sum_{i,j} \sqrt{(\delta_x f_{i,j})^2 + (\delta_y(f_{i,j} - g_j))^2} + \lambda \|g(y)\|_1 \right\}$$

*B. Augmented Lagrangian*

1) *Anisotropic*: With the discrete forward difference approximation matrix defined above, we can rewrite the minimization problem as:

$$\textit{Point Form: } \min_{\vec{g}} \left\{ \sum_{i,j} |\delta_y(f_{i,j} - g_j)| + \lambda \|g(y)\|_1 \right\}$$

$$\textit{Vector Form: } \min_{\vec{g}} \left\{ \sum_i \|D(f_i - \vec{g})\|_1 + \lambda \|g(y)\|_1 \right\}$$

$$\textit{Matrix Form: } \min_{\vec{g}} \left\{ \|D(f - \vec{g} \otimes \mathbf{1}_{\vec{C}})\|_{1,1} + \lambda \|g(y)\|_1 \right\}$$

To render the constrained minimization problem unconstrained, we introduce auxiliary variables, Lagrangian multipliers (split Bregman), and quadratic penalty terms, so that the augmented Lagrangian is defined as:

$$\begin{aligned} \mathcal{L}_{\alpha,\lambda}(b_i, h, g, q_i, r) &= \sum_i \left( \|b_i\|_1 + \frac{\alpha}{2} \|b_i - D(g - f_i)\|_2^2 + \langle q_i, b_i - D(g - f_i) \rangle \right) \\ &\quad + \lambda \left( \|h\|_1 + \frac{\alpha}{2} \|h - g\|_2^2 + \langle r, h - g \rangle \right) \\ &= \sum_i \left( \|b_i\|_1 + \frac{\alpha}{2} \|b_i - D(g - f_i) + \frac{q_i}{\alpha}\|_2^2 \right) \\ &\quad + \lambda \left( \|h\|_1 + \frac{\alpha}{2} \|h - g + \frac{r}{\alpha}\|_2^2 \right) + \mathcal{O}(q_i^2, r^2) \end{aligned}$$

We now solve the unconstrained saddle point problem.

$$\min_{b_i, h, g} \max_{q_i, r} \mathcal{L}_{\alpha,\lambda}(b_i, h, g, q_i, r)$$

The solution to the original constrained minimization problem is now found as the saddle point of the augmented Lagrangian  $\mathcal{L}$  in a sequence of iterative sub-optimizations called alternating direction method of multipliers (ADMM) [21], [22], [23], [24], [25], [26].

The splitting variables  $b_i$ , and  $h$  are updated by the proximal mapping operator:

$$\begin{aligned}
b_i^{k+1} &= \arg \min_{b_i} \mathcal{L}_{\alpha, \lambda}(b_i, h^k, g^k, q_i^k, r^k) \\
&= \arg \min_{b_i} \left\{ \|b_i\|_1 + \frac{\alpha}{2} \|b_i - D(g - f_i) + \frac{q_i}{\alpha}\|_2^2 \right\} \\
&= S_{\frac{1}{\alpha}} \left( D(g - f_i) - \frac{q_i}{\alpha} \right) \\
h^{k+1} &= \arg \min_h \mathcal{L}_{\alpha, \lambda}(b_i^{k+1}, h, g^k, q_i^k, r^k) \\
&= \arg \min_{h_i} \left\{ \|h\|_1 + \frac{\alpha}{2} \|h - g\|_2^2 \right\} \\
&= S_{\frac{1}{\alpha}} \left( g - \frac{r}{\alpha} \right)
\end{aligned}$$

Due to the introduction of the splitting variables,  $g$  is only contained in quadratic terms, and thus easily solved for:

$$\begin{aligned}
g^{k+1} &= \arg \min_g \mathcal{L}_{\alpha, \lambda}(b_i^{k+1}, h^{k+1}, g, q_i^k, r^k) \\
&= \arg \min_g \left\{ \frac{\alpha}{2} \sum_i \|b_i - D(g - f_i) + \frac{q_i}{\alpha}\|_2^2 \right. \\
&\quad \left. + \frac{\lambda\alpha}{2} \|h - g + \frac{r}{\alpha}\|_2^2 \right\} \Rightarrow
\end{aligned}$$

$$\begin{aligned}
\frac{\delta \mathcal{L}}{\delta g} &= \alpha \sum_i -D^T (b_i - D(g - f_i) + \frac{q_i}{\alpha}) - \lambda\alpha (h - g + \frac{r}{\alpha}) = \\
\alpha(CD^T D + \lambda I)g - \alpha D^T (\sum_i b_i + Df_i + \frac{q_i}{\alpha}) - \lambda\alpha h + \lambda r &= 0 \Rightarrow \\
g &= (CD^T D + \lambda I)^{-1} \left( D^T (\sum_i b_i + Df_i + \frac{q_i}{\alpha}) + \lambda (h - \frac{r}{\alpha}) \right)
\end{aligned}$$

The Lagrangian multipliers (split Bregman variables) are updated through gradient ascent.

$$\begin{aligned}
q_i^{k+1} &= q_i^k + \tau\alpha (b_i^{k+1} - D(g^{k+1} - f_i)) \\
r^{k+1} &= r^k + \tau\lambda\alpha (h^{k+1} - g^{k+1})
\end{aligned}$$

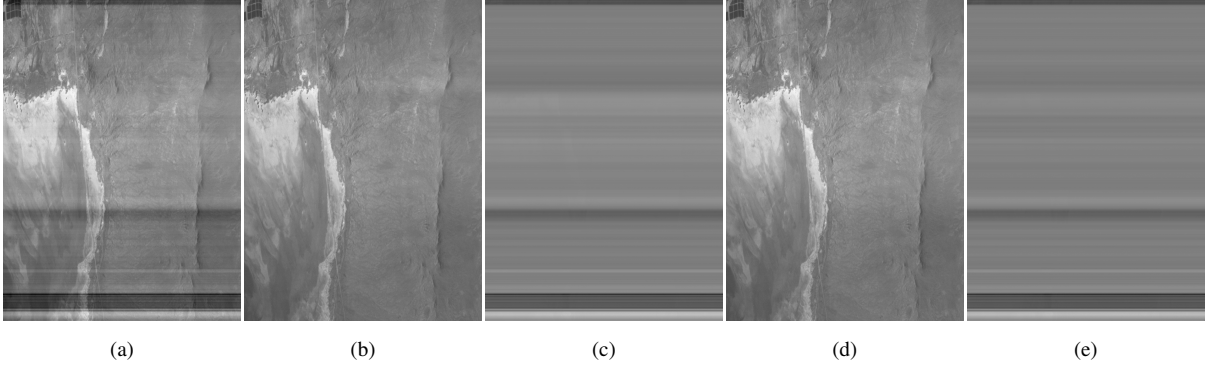


Fig. 2: (a) The 355 nm channel image with stripes captured by AirMSPI instrument from Nadir angle at Mojave, California. (b) Destriped image using TV- $L^2$  model. (c) Difference between captured image from (a) and TV- $L^2$  destriped image from (b). (d) Destriped image using TV- $L^1$  model. (e) Difference between captured image from (a) and TV- $L^1$  destriped image from (d).

2) *Isotropic*: Due to the coupling of the terms in this version of the minimization problem, we cannot compactly write the problem with matrices as above; however, the solution is just as readily available. Here the  $\diamond$  denotes the Hadamard matrix power operator, which acts pointwise on the matrix.

*Point Form*:

$$\min_{\vec{g}} \left\{ \sum_{i,j} \sqrt{(\delta_x f_{i,j})^2 + (\delta_y (f_{i,j} - g_j))^2} + \lambda \|g(y)\|_1 \right\}$$

*Matrix Form*:

$$\min_{\vec{g}} \left\{ \|[(fD^T)^{\diamond 2} + (D(f - \vec{g} \otimes \vec{1}_C))^{\diamond 2}]^{\diamond \frac{1}{2}}\|_{1,1} + \lambda \|g(y)\|_1 \right\}$$

Just as before, we introduce splitting variables and Lagrangian multipliers to form the augmented Lagrangian:

$$\begin{aligned} \mathcal{L}_{\alpha,\lambda}(a_{i,j}, b_{i,j}, h, g, p_{i,j}, q_{i,j}, r) &= \sum_{i,j} \sqrt{|a_{i,j}|^2 + |b_{i,j}|^2} + \frac{\alpha}{2} \|a_{i,j} - \delta_x f_{i,j}\|_2^2 + \langle p_{i,j}, a_{i,j} - \delta_x f_{i,j} \rangle \\ &\quad + \frac{\alpha}{2} \|b_{i,j} - \delta_y (f_{i,j} - g_j)\|_2^2 + \langle q_{i,j}, b_{i,j} - \delta_y (f_{i,j} - g_j) \rangle \\ &\quad + \lambda (\|h\|_1 + \frac{\alpha}{2} \|h - g\|_2^2 + \langle r, h - g \rangle) \\ &= \sum_{i,j} \sqrt{|a_{i,j}|^2 + |b_{i,j}|^2} + \frac{\alpha}{2} \|a_{i,j} - \delta_x f_{i,j} + \frac{p_{i,j}}{\alpha}\|_2^2 \\ &\quad + \frac{\alpha}{2} \|b_{i,j} - \delta_y (f_{i,j} - g_j) + \frac{q_{i,j}}{\alpha}\|_2^2 \\ &\quad + \lambda (\|h\|_1 + \frac{\alpha}{2} \|h - g + \frac{r}{\alpha}\|_2^2) \\ &\quad + \mathcal{O}(q_{i,j}^2, p_{i,j}^2, r^2) \end{aligned}$$

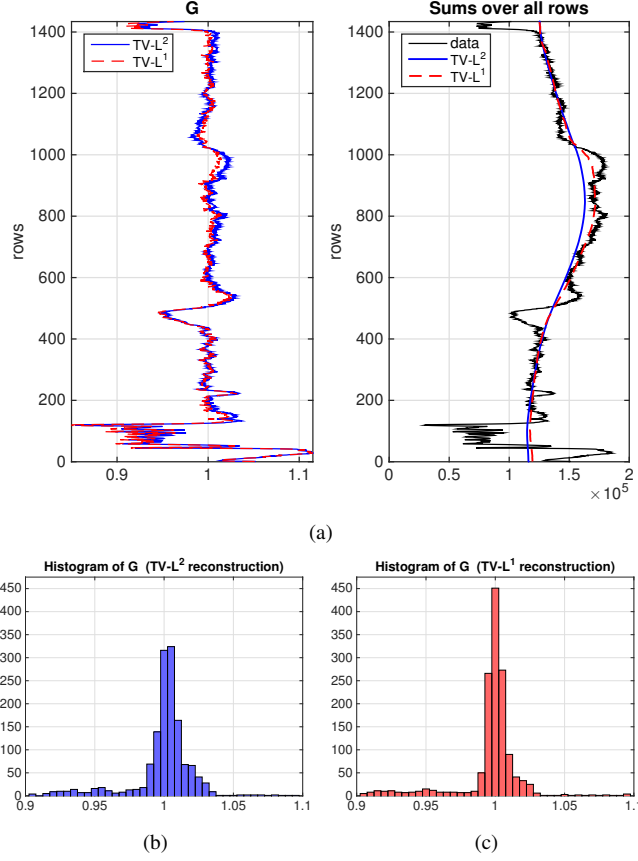


Fig. 3: Comparisons of TV- $L^2$  and TV- $L^1$  destriping for the results shown in Fig. 2. (a) On the left, plots of recovered function  $G$  for TV- $L^2$  destriped image (blue) and TV- $L^1$  destriped image (red) are shown. On the right, plots of sums over all rows of original image with stripes (black), TV- $L^2$  destriped image (blue), and TV- $L^1$  destriped image (red) are shown. (b) Histogram of function  $G$  for TV- $L^2$  reconstruction. (c) Histogram of function  $G$  for TV- $L^1$  reconstruction.

The splitting variables  $a_{i,j}$ ,  $b_{i,j}$  are updated by the vectorial proximal mapping operator:

$$\begin{aligned}
 \langle a_{i,j}, b_{i,j} \rangle &= \arg \min_{\langle a_{i,j}, b_{i,j} \rangle} \mathcal{L}_{\alpha, \lambda}(a_{i,j}, b_{i,j}, h^k, g^k, p_i^k, q^k) \\
 &= \arg \min_{\langle a_{i,j}, b_{i,j} \rangle} \left\{ \sqrt{|a_{i,j}|^2 + |b_{i,j}|^2} + \frac{\alpha}{2} \|a_{i,j} - \delta_x f_{i,j} + \frac{p_{i,j}}{\alpha}\|_2^2 \right. \\
 &\quad \left. + \frac{\alpha}{2} \|b_{i,j} - \delta_y(f_{i,j} - g_j) + \frac{q_{i,j}}{\alpha}\|_2^2 \right\} \\
 &= \arg \min_{\langle a_{i,j}, b_{i,j} \rangle} \left\{ \|\langle a_{i,j}, b_{i,j} \rangle\| + \frac{\alpha}{2} \|\langle a_{i,j}, b_{i,j} \rangle - \langle \delta_x f_{i,j} + \frac{p_{i,j}}{\alpha}, \delta_y(f_{i,j} - g_j) + \frac{q_{i,j}}{\alpha} \rangle\|^2 \right\} \\
 &= S_{\frac{1}{\alpha}} \left( \langle \delta_x f_{i,j} + \frac{p_{i,j}}{\alpha}, \delta_y(f_{i,j} - g_j) + \frac{q_{i,j}}{\alpha} \rangle \right)
 \end{aligned}$$

Each component of the vector is updated via shrinkage as follows:

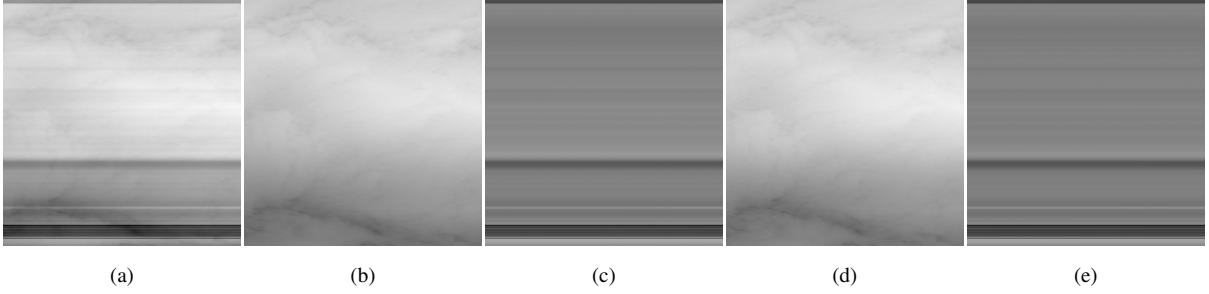


Fig. 4: (a) The 355 nm channel image with stripes depicting clouds over the Pacific Ocean captured by AirMSPI instrument from  $66.0^\circ$ F angle. (b) Destriped image using TV- $L^2$  model. (c) Difference between captured image from (a) and TV- $L^2$  destriped image from (b). (d) Destriped image using TV- $L^1$  model. (e) Difference between captured image from (a) and TV- $L^1$  destriped image from (d).

$$a_{i,j} = \frac{\delta_x f_{i,j} + \frac{p_{i,j}}{\alpha}}{s} \cdot \max\left(s - \frac{1}{\alpha}, 0\right)$$

$$b_{i,j} = \frac{\delta_y (f_{i,j} - g_j) + \frac{q_{i,j}}{\alpha}}{s} \cdot \max\left(s - \frac{1}{\alpha}, 0\right)$$

$$s = \sqrt{\left(\delta_x f_{i,j} + \frac{p_{i,j}}{\alpha}\right)^2 + \left(\delta_y (f_{i,j} - g_j) + \frac{q_{i,j}}{\alpha}\right)^2}$$

The splitting variable  $h$ , the striping mask  $g$ , and the Lagrangian multipliers are updated as before due to the common structure between the two models.

$$p_{i,j}^{k+1} = p_{i,j}^k + \tau\alpha(\delta_x f_{i,j} + \frac{p_{i,j}}{\alpha})$$

### C. TV- $L^2$ ADMM

We introduce a slight variant to the TV- $L^1$  model where the norm on the striping mask is replaced by an  $L_2$  norm, this is called the TV- $L^2$  model.

$$\min_g \left\{ \sum_{i,j} \|\langle \delta_x f_{i,j}, \delta_y (f_{i,j} - g_j) \rangle\|_1 + \frac{\lambda}{2} \|g(y)\|_2^2 \right\}$$

In both the isotropic and anisotropic cases, the energy terms with  $g$  in the augmented Lagrangians are the same:

$$\begin{aligned} & \sum_{i,j} \frac{\alpha}{2} \|b_{i,j} - \delta_y(f_{i,j} - g_j) + \frac{q_{i,j}}{\alpha}\|_2^2 + \frac{\lambda}{2} \|g\|_2^2 = \\ & \sum_i \frac{\alpha}{2} \|b_i - D(g - f_i) + \frac{q_i}{\alpha}\|_2^2 + \frac{\lambda}{2} \|g\|_2^2 \end{aligned}$$

$$\begin{aligned} g^{k+1} &= \arg \min_g \mathcal{L}_{\alpha,\lambda}(b_i^{k+1}, h^{k+1}, g, p_i^k, q_i^k, r^k) \\ &= \arg \min_g \left\{ \frac{\alpha}{2} \sum_i \|b_i - D(g - f_i) + \frac{q_i}{\alpha}\|_2^2 + \frac{\lambda}{2} \|g\|_2^2 \right\} \Rightarrow \\ \frac{\delta \mathcal{L}}{\delta g} &= \alpha \sum_i -D^T(b_i - D(g - f_i) + \frac{q_i}{\alpha}) + \lambda g \\ &= (\alpha C D^T D + \frac{\lambda}{\alpha} I)g - \alpha D^T(\sum_i b_i + D f_i + \frac{q_i}{\alpha}) = 0 \Rightarrow \\ g &= (C D^T D + \frac{\lambda}{\alpha} I)^{-1} \left( D^T(\sum_i b_i + D f_i + \frac{q_i}{\alpha}) \right) \end{aligned}$$

The quadratic penalty on the size of the striping mask is included for comparison with the  $L_1$  penalty term. Given the same parameters  $\alpha$ , and  $\lambda$ , the TV- $L^1$  should be able to remove deeper stripes (of higher magnitude) while preserving small fluctuations (of lesser magnitude) by not classifying them as stripes. We compare both the TV- $L^1$  and TV- $L^2$  models in our experiments.

The first algorithm (anisotropic) is presented in vector fashion. The second algorithm (isotropic) is presented in matrix fashion.

## V. ALGORITHM

Algorithm 1: Complete ADMM optimization of TV- $L^1$

- 1: Initialize:  $A^0 = (\vec{a}_i)$ ,  $B^0 = (\vec{b}_i)$ ,  $Q^0 = (\vec{q}_i) \leftarrow 0 \in \mathbb{R}^{R \times C}$ ,  $g^0, h^0, r^0 \leftarrow 0 \in \mathbb{R}^{R \times 1}$ ,  $n \leftarrow 0 \in \mathbb{R}$
- 2:  $f = (\vec{f}_i) \leftarrow \ln(F)$ ,  $D \leftarrow 0 \in \mathbb{R}^{R \times R}$ ,  $(D)_{i,i} = -1$ ,  $(D)_{i,i+1} = 1$  for  $i = 1, \dots, R - 1$
- 3: **repeat**
- 4:      $n \leftarrow n + 1$
- 5:     **case** Anisotropic:
- 6:         **for**  $i = 1 : C$  **do**
- 7:     Update splitting variable for smoothness regularizer term via shrinkage:
- 8:

$$\vec{b}_i^{n+1} \leftarrow S_{\frac{1}{\alpha}} \left( D(\vec{g}^n - \vec{f}_i) - \frac{\vec{q}_i^n}{\alpha} \right)$$

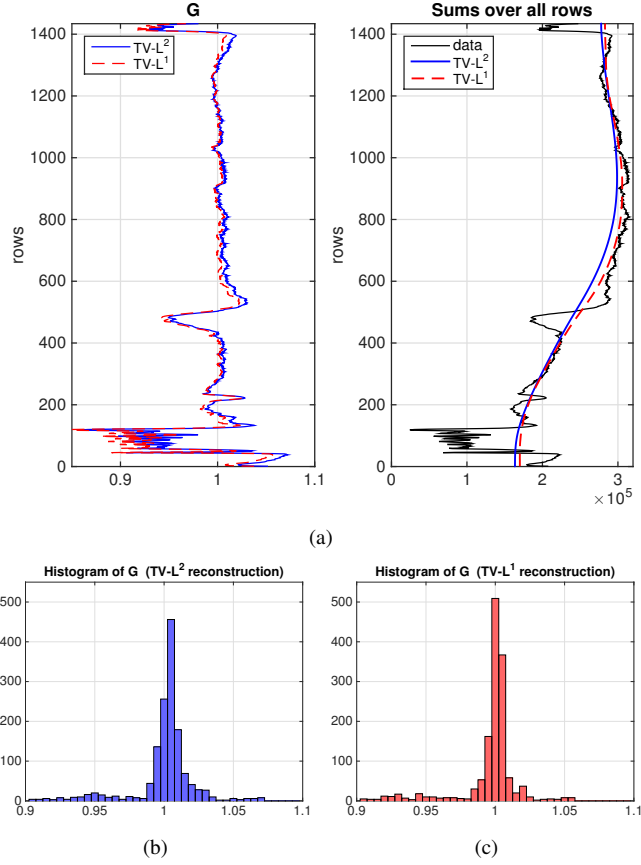


Fig. 5: Comparisons of TV- $L^2$  and TV- $L^1$  destriping for the results shown in Fig. 4. (a) On the left, plots of recovered function  $G$  for TV- $L^2$  destriped image (blue) and TV- $L^1$  destriped image (red) are shown. On the right, plots of sums over all rows of original image with stripes (black), TV- $L^2$  destriped image (blue), and TV- $L^1$  destriped image (red) are shown. (b) Histogram of function  $G$  for TV- $L^2$  reconstruction. (c) Histogram of function  $G$  for TV- $L^1$  reconstruction.

9: Update Lagrangian multiplier for regularizer term via dual ascent:

$$\vec{q}_i^{n+1} \leftarrow \vec{q}_i^n + \tau\alpha(\vec{b}_i^{\vec{n}+1} - D(\vec{g}^n - \vec{f}_i))$$

10: **end for**

11: **case** Isotropic:

12: **for**  $i = 1 : C, j = 1 : R$  **do**

13: Update splitting variables for smoothness regularizer term via vectorial shrinkage:

$$\langle a_{i,j}^{n+1}, b_{i,j}^{n+1} \rangle \leftarrow S_{\frac{1}{\alpha}}(\langle \delta_x f_{i,j} + \frac{p_{i,j}^n}{\alpha}, \delta_y(f_{i,j} - g_j^n) + \frac{q_{i,j}^n}{\alpha} \rangle)$$

14: Update Lagrangian multipliers for regularizer term via dual ascent:

15:

$$p_{i,j}^{n+1} \leftarrow p_{i,j}^n + \tau\alpha(\delta_x f_{i,j} + \frac{p_{i,j}}{\alpha})$$

$$q_{i,j}^{n+1} \leftarrow q_{i,j}^n + \tau\alpha(b_{i,j}^{n+1} - \delta_y(g_j^n - f_{i,j}))$$

16: **end for**17: **case TV- $L^1$ :**

18: Update splitting variable for data fidelity term via shrinkage:

19:

$$\vec{h}^{n+1} \leftarrow S_{\frac{\lambda}{\alpha}} \left( \vec{g}^n - \frac{\vec{r}^n}{\alpha} \right)$$

20: Update striping mask:

21:

$$\vec{g}^{n+1} \leftarrow (CD^T D + \lambda I)^{-1} \left( D^T \left( \sum_i \vec{b}_i^{\vec{r}^{n+1}} + D\vec{f}_i + \frac{\vec{q}_i^{\vec{r}^{n+1}}}{\alpha} \right) + \lambda \vec{h}^{n+1} - \frac{\lambda}{\alpha} \vec{r}^n \right)$$

22: Update Lagrangian multiplier for data fidelity term via dual ascent:

23:

$$\vec{r}^{n+1} \leftarrow \vec{r}^n + \tau\lambda\alpha(\vec{h}^{n+1} - \vec{g}^{n+1})$$

24: **case TV- $L^2$ :**

25: Update striping mask:

$$\vec{g}^{n+1} \leftarrow (CD^T D + 2\frac{\lambda}{\alpha} I)^{-1} \left( D^T \left( \sum_i \vec{b}_i^{\vec{r}^{n+1}} + D\vec{f}_i + \frac{\vec{q}_i^{\vec{r}^{n+1}}}{\alpha} \right) \right)$$

Update energy terms:

$$E_1^{n+1} \leftarrow \sum_i \|D(\vec{f}_i - \vec{g}^{n+1})\|_1, \quad E_2^{n+1} \leftarrow \lambda \|\vec{g}^{n+1}\|_1$$

$$E^{n+1} \leftarrow E_1^{n+1} + E_2^{n+1}$$

26: **until** convergence:27:  $\|\vec{g}^{n+1} - \vec{g}^n\|_2^2 / \|\vec{g}^n\|_2^2 < \epsilon_g$  and  $|E^{n+1} - E^n|^2 / |E^n|^2 < \epsilon_E$ .

28: Retrieve clean image:

$$u \leftarrow f - g^{n+1} \otimes [1_1, 1_2, \dots, 1_C]$$

$$U \leftarrow \exp(u)$$

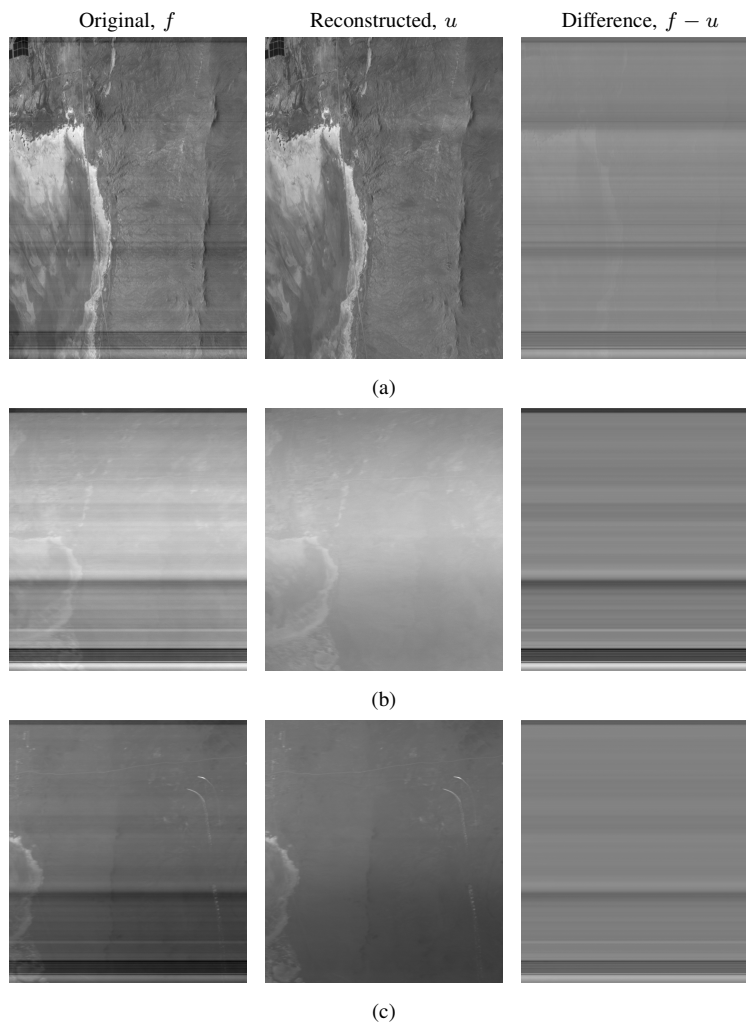


Fig. 6: Images with stripes captured by AirMSPI instrument at Mojave, California (left), destriped images using TV- $L^1$  model (center), and differences between captured and destriped images (right) are shown. The bands and viewing angles are: (a) 380 nm band at Nadir angle; (b) 355 nm band at  $66.1^\circ$ F angle; (c) 355 nm band at  $66.1^\circ$ A angle. 355 nm band at Nadir angle is shown in Fig. 2.

## VI. EXPERIMENTS

In our experiments, we used data acquired by the Airborne Multi-angle Spectro Polarimetric Imager (AirMSPI). AirMSPI is an airborne prototype instrument similar to that of the future satellite-borne MSPI instrument for obtaining multi-angle polarization imagery [27]. The instrument was built for NASA by the Jet Propulsion Laboratory in Pasadena, California and has been flying aboard the NASA ER-2 high altitude aircraft since October 2010.

AirMSPI is an eight-band (355, 380, 445, 470, 555, 660, 865, 935 nm) pushbroom camera, measuring polarization

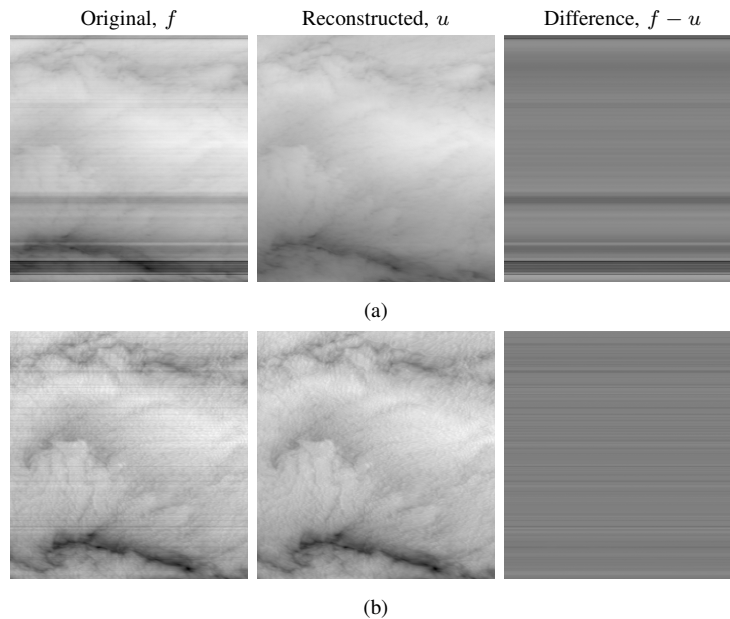


Fig. 7: Images with stripes depicting clouds over the Pacific Ocean captured by AirMSPI instrument (left), destriped images using  $TV-L^1$  model (center), and differences between captured and destriped images (right) are shown. The bands are: (a) 380 nm, and (b) 660 nm all at  $66.0^\circ\text{F}$ . 355 nm band at  $66.0^\circ\text{F}$  angle is shown in Fig. 4.

in the 470, 660, and 865 nm bands, mounted on a gimbal to acquire multiangular observations over a  $\pm 67^\circ$  along-track range. Two principal observing modes are employed: step-and-stare, in which 11 km x 11 km targets are observed at a discrete set of view angles with a spatial resolution of  $\sim 10$  m; and continuous sweep, in which the camera slews back and forth along the flight track between  $\pm 67^\circ$  to acquire wide area coverage (11 km swath at nadir, target length 108 km) with  $\sim 25$  m spatial resolution. Step-and-stare provides more angles, but continuous sweep gives greater coverage. Multiple observing modes can be programmed into the instrument and activated under cockpit control. Multiangle radiance and polarization imagery from AirMSPI will provide 3-D scene context where clouds and aerosol plumes are present. It will also enable retrieval of aerosol and cloud macrophysical properties (distribution, height), microphysical properties (size distribution, single scattering albedo, shape), and optical depth.

We first compare destriping results generated using  $TV-L^2$  and  $TV-L^1$  models. Fig. 2 shows the 355 nm UV channel image with stripes captured by the AirMSPI instrument from Nadir angle at Mojave, California. The image is destriped using  $TV-L^2$  and  $TV-L^1$  models. As we see from the destriped images and corresponding differences between captured images and destriped images,  $TV-L^2$  model does not preserve radiometric intensities in regions where no stripes are present. Fig. 3(a,left) shows plots of recovered function  $g$  for  $TV-L^2$  and  $TV-L^1$  destriped images.  $TV-L^1$  recovered function  $g$  is closer to identity especially at the rows where with no stripes,

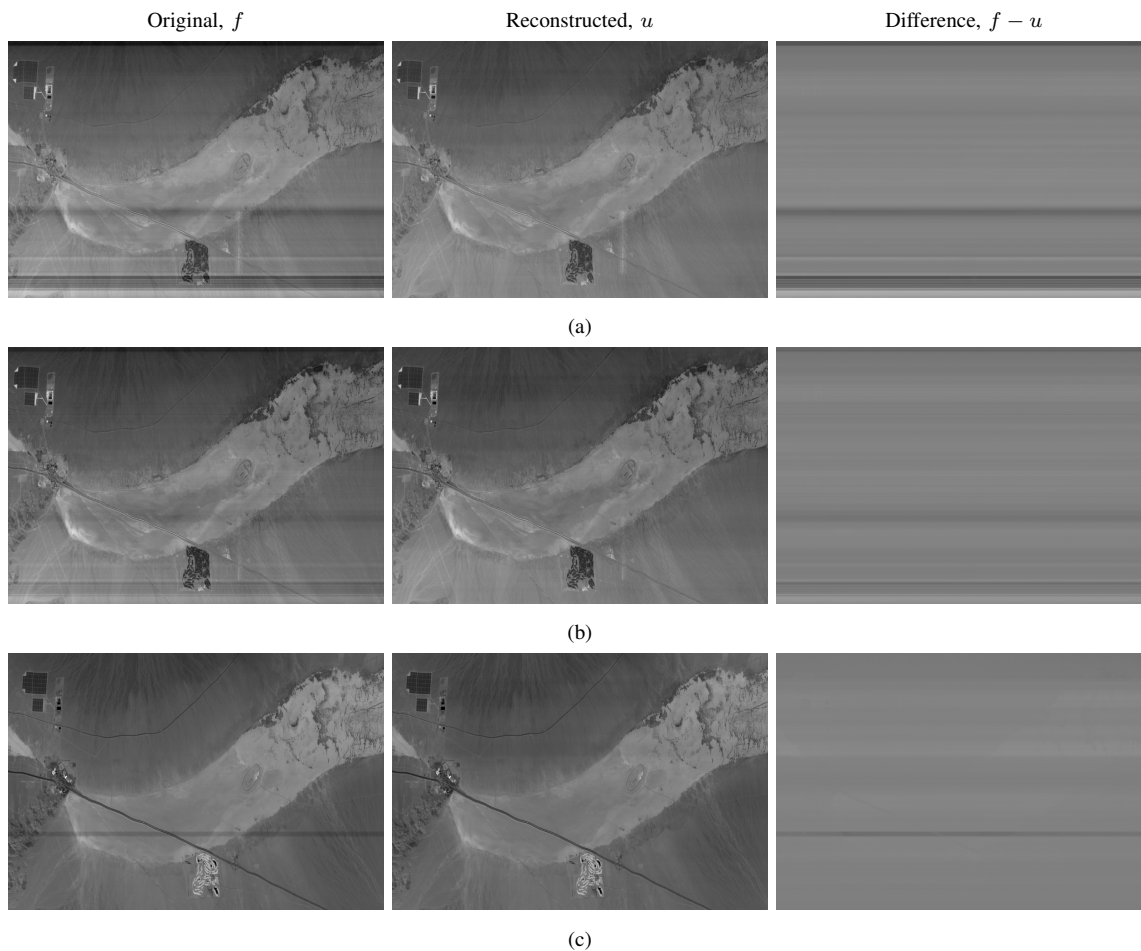


Fig. 8: Images with stripes of dry lake Ivanpah, California captured by AirMSPI instrument (left), destriped images using  $TV-L^1$  model (center), and differences between captured and destriped images (right) are shown. The bands are: (a) 355 nm, (b) 380 nm, and (c) 865 nm bands, all at Nadir angle.

suggesting  $TV-L^1$  reconstruction is more accurate than  $TV-L^2$  reconstruction. Fig. 3(a,right) shows plots of sums over all rows of the original image with stripes (from Fig. 2), as well as sums of rows for  $TV-L^2$  and  $TV-L^1$  destriped images. These plots indicate that  $TV-L^1$  model preserves radiometric intensities of the original images better, which  $TV-L^2$  model produces more artificial smoothing throughout the image. Figures 3 (b) and (c) show histograms of function  $g$  for  $TV-L^2$  and  $TV-L^1$  reconstructions, respectively.  $TV-L^1$  reconstruction is pointier than  $TV-L^2$  reconstruction. It is also centered at 1, as opposed to  $TV-L^2$  reconstruction, which further indicates better accuracy of  $TV-L^1$  model. Note that the actual stripes, at around  $g \approx 0.95$  are represented in the histograms by small bumps.

Fig. 4 and Fig. 5 display similar results as in Fig. 2 and 3 for the 355 nm channel image with stripes depicting

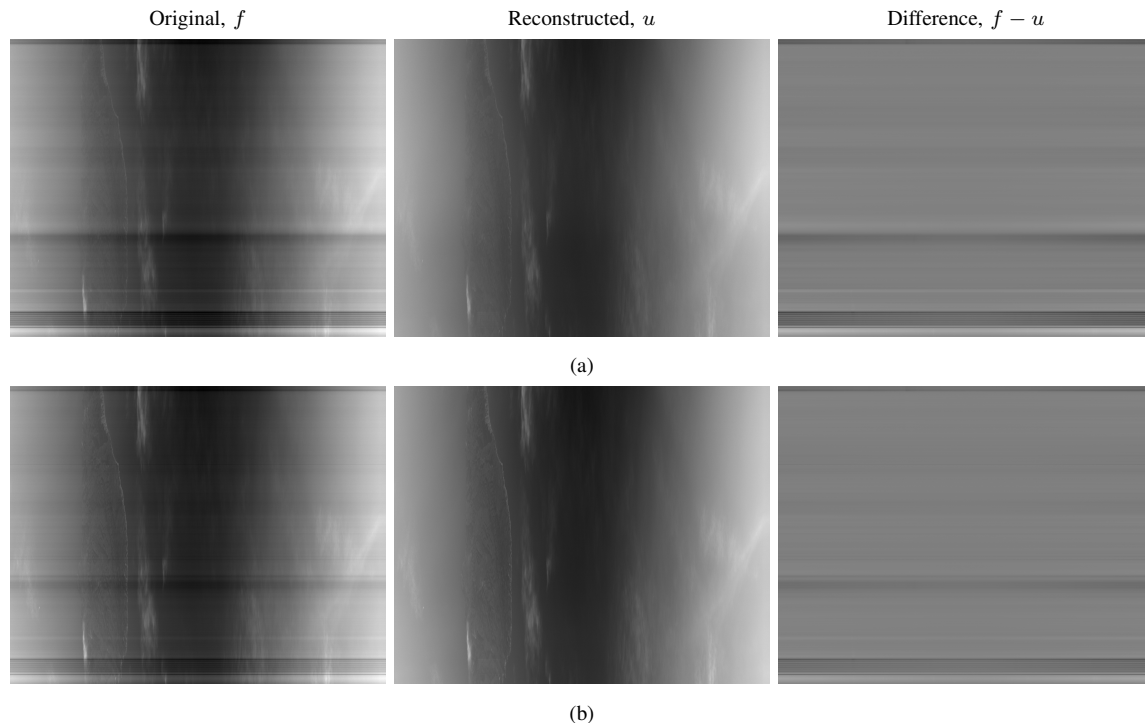


Fig. 9: Images captured by AirMSPI instrument at Avalon, California (left), destriped images using TV- $L^1$  model (center), and differences between captured and destriped images (right) are shown. The bands are: (a) 355 nm and (b) 380 nm, both captured using the continuous sweep observing mode.

clouds over the Pacific Ocean captured by AirMSPI instrument from 66.0°F angle.

Figures 6, 7, and 8 show more examples of TV- $L^1$  reconstruction of images captured using continuous sweep observing mode. Figures 9 and 10 display images captured using the step-and-stare observing mode as well as destriped results using TV- $L^1$  model.

## VII. CONCLUSION

In this paper, we have presented a novel variational method for image destriping through fast minimization techniques of appropriately modelled energy functionals - namely total variation and  $L^1$  data fidelity term. In contrast to existing destriping models, such as statistical estimation models, we simplify the calculations while achieving excellent qualitative results quickly and with few explicit parameters.

Our destriping model solves the inverse problem as follows: minimally remove a univariate multiplicative striping mask from the data, such that the clean image is somewhat smooth and the removed stripe has low energy. We assess the smoothness of the clean image using total variation, which maintains sharp image features and preserves

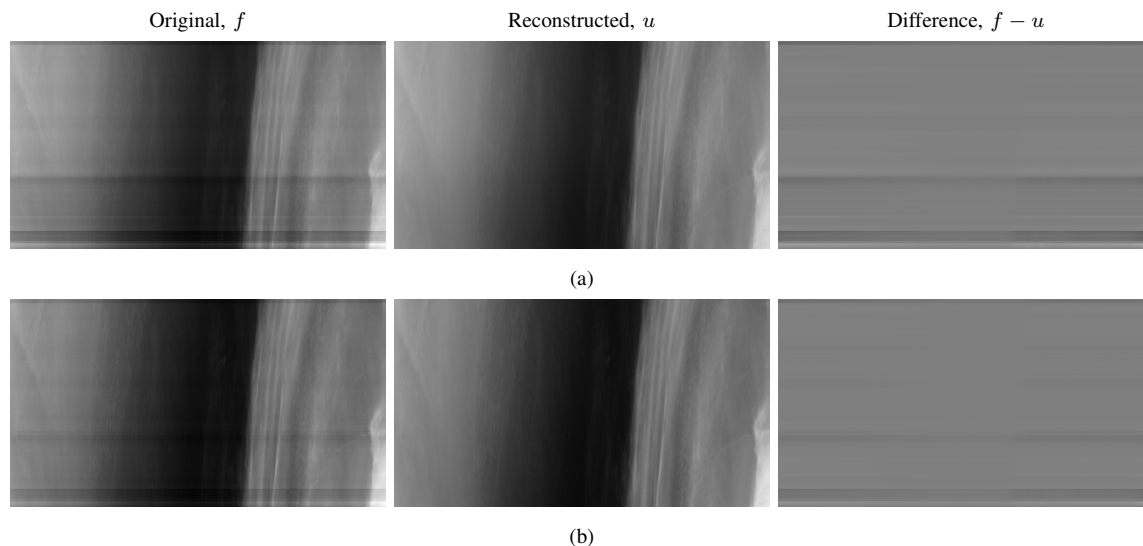


Fig. 10: Images with stripes captured by AirMSPI instrument at Fallbrook, California (left), destriped images using TV- $L^1$  model (center), and differences between captured and destriped (right) are shown. The bands are: (a) 355 nm and (b) 380 nm, both captured using the continuous sweep observing mode.

definition and contrast. We address both isotropic and anisotropic total variation in this paper, each having their respective strengths and weaknesses. We use  $L^1$ , and for comparison,  $L^2$  energy to measure the removed striping, ensuring minimal data removal and thus a clean image of high fidelity.

The variational problem is solved very efficiently in an ADMM approach: introduce splitting variables and quadratic penalties for deviations from said splitting variables to allow efficient optimization via proximal shrinkage operators, explicit quadratic solutions, and simple gradient ascent for the Lagrangian multipliers. In our experiments, we have shown that the proposed method yields qualitatively good results, removes very minimal masking, and does so quickly in both iterations and time. From the histogram distributions of  $G$ , we observe a narrower spread around 1, yet a wider, more equidistributed support, suggesting that most of the time, there is minimal masking removal (multiplier close to 1), yet in areas of heavy striping, the destriping effect is more prevalent and of greater magnitude.

Applications of this algorithm are not limited to satellite imagery, and may be analogized to other fields such as raster scans in microscopy. Any scientific measurements (of images) made mostly along a curve – parameterizable by a single dimension – may be susceptible to such striping biases, and may be a candidate for similar destriping. Future work will expand this model to multi-modal images, color images, and may incorporate other specific priors on the data.

## VIII. ACKNOWLEDGEMENT

The authors would like to thank Andrea Bertozzi, Michael Bull, David Diner, Michael Garay, Veljko Jovanovic, Stanley Osher, Brian Rheingans, Luminita Vese, and Dominique Zosso for their helpful comments and discussions. The authors also thank the AirMSPI team for providing data for our experiments.

## REFERENCES

- [1] H. Carfantan, and J. Idier, Statistical Linear Destriping of Satellite-Based Pushbroom-Type Images, *IEEE Trans. Geosci. Remote Sens.*, vol. 48, no. 4, pp. 1860–1871, Mar. 2010.
- [2] H. Shen, and L. Zhang, A MAP-based algorithm for destriping and inpainting of remotely sensed images, *IEEE Trans. Geosci. Remote Sens.*, vol. 47, no. 5, pp. 1492–1502, May. 2009.
- [3] R. Srinivasan, and M. C. J. White, Landsat data destriping using power spectral filtering, *Opt. Eng.*, vol. 27, no. 11, pp. 939-943, Nov. 1988.
- [4] R. E. Crippen, A simple spatial filtering routine for the cosmetic removal of scan-line noise from LANDSAT TM P-tape imagery, *Photogramm. Eng. Remote Sens.*, vol. 55, no. 3, pp. 327-331, Mar. 1989.
- [5] D. L. Helder, B. K. Quirk, and J. J. Hood, A technique for the reduction of banding in LANDSAT Thematic Mapper images, *Photogramm. Eng. Remote Sens.*, vol. 58, no. 10, pp. 1425-1431, Oct. 1992.
- [6] J. J. Simpson, J. R. Stitt, and D. M. Leath, Improved finite impulse response filters for enhanced destriping of geostationary satellite data, *Opt. Eng.*, vol. 66, no. 3, pp. 235-249, Dec. 1998.
- [7] J. Chen, Y. Shao, H. Guo, W. Wang, and B. Zhu, Destriping CMODIS data by power filtering, *IEEE Trans. Geosci. Remote Sens.*, vol. 41, no. 9, pp. 2119-2124, Sep. 2003.
- [8] J. Torres and S. O. Infante, Wavelet analysis for the elimination of striping noise in satellite images, *Opt. Eng.*, vol. 40, no. 7, pp. 1309-1314, Jul. 2001.
- [9] J. Chen, H. Lin, Y. Shao, and L. Yang, Oblique striping removal in remote sensing imagery based on wavelet transform, *Int. J. Remote Sens.*, vol. 27, no. 8, pp. 1717-1723, Apr. 2006.
- [10] P. Rakwatin, W. Takeuchi, and Y. Yasuoka, Stripe noise reduction in MODIS data by combining histogram matching with facet filter, *IEEE Trans. Geosci. Remote Sens.*, vol. 45, no. 6, pp. 1844-1856, Jun. 2007.
- [11] J. A. Dobrosotskaya, and A. L. Bertozzi, A Wavelet-Laplace Variational Technique for Image Deconvolution and Inpainting, *IEEE Transactions on Image Processing*, vol. 17, no. 5, pp. 657–663, 2008.
- [12] T.F. Chan, and L.A. Vese, Active Contours Without Edges, *IEEE Transactions on Image Processing*, vol. 10, no. 2, pp. 266–277, 2001.
- [13] Y. Chang, H. Fang, L. Yan, and H. Liu, Robust destriping method for unidirectional total variation and framelet regularization, *Optics Express*, vol. 21, no. 20, pp. 23307-23323, 2013.

- [14] Y. Chang, L. Yan, H. Fang, and C. Luo, Anisotropic Spectral-Spatial Total Variation Model for Multispectral Remote Sensing Image Destriping, *IEEE Transactions on Image Processing*, vol. 24, no. 6, pp. 1852-1866, 2015.
- [15] A.N. Tikhonov, and V.Y. Arsenin, Solutions of Ill-posed Problems, *Winston and Sons, Washington*, 1977.
- [16] B. Muench, P. Trtik, F. Marone, and M. Stampanoni, Stripe and ring artifact removal with combined wavelet-Fourier filtering, *Optics Express*, vol. 17, no. 10, pp. 8567-8591, 2009.
- [17] L. I. Rudin, S. Osher, and E. Fatemi, A Nonlinear total variation based noise removal algorithms , *Physica D*. vol. 60, pp. 256-268.
- [18] L. Rudin and S. Osher, Total variation based image restoration with free local constraints, *IEEE International Conference on Image Processing*, vol. 1, pp. 31-35, 1994.
- [19] D. L. Donoho and I.M. Johnstone, Adapting to unknown smoothness via wavelet shrinkage, *J. Amer. Stat. Assoc.*, vol. 90, no. 432, pp. 1200-1224, 1995.
- [20] Y. Wang, W. Yin, and Y. Zhang, A fast algorithm for image deblurring with total variation regularization, Rice Univ., Houston, Texas, USA, CAAM Tech. Rep. TR07-10, 2007.
- [21] R.T. Rockafeller, A dual approach to solving nonlinear programming problems by unconstrained optimization, *Mathematical Programming*, vol. 5, no. 1, pp. 354-373, 1973.
- [22] R. Glowinski and A. Marrocco, Sur l'approximation, par elements finis d'ordre un, et la resolution, par, penalisation-dualité, d'une classe de problems de Dirichlet non lineares, *Revue Française d'Automatique, Informatique, et Recherche Opérationnelle*, vol. 9, pp. 41-76, 1975.
- [23] D. Gabay and B. Mercier, A dual algorithm for the solution of nonlinear variational problems via finite element approximations, *Computers and Mathematics with Applications*, vol. 2, pp. 17-40, 1976.
- [24] M. R. Hestenes, Multiplier and Gradient Methods, *Journal of Optimization Theory and Applications.*, vol. 4, no. 5, pp. 303-320, 1969.
- [25] Y. Wang, J. Yang, W. Yin, and Y. Zhang, A new alternating minimization algorithm for total variation image reconstruction, *SIAM J. Imaging Sci.*, vol. 1, no. 3, pp. 248-272, 2008.
- [26] T. Goldstein and S. Osher, The split bregman method for L1 regularized problems, *SIAM Journal of Imaging Science*, vol. 2, no. 2, pp. 323-343, 2009.
- [27] D. J. Diner, F. Xu, M. J. Garay, J. V. Martonchik, B. E. Rheingans, S. Geier, A. Davis, B. R. Hancock, V. M. Jovanovic, M. A. Bull, K. Capraro, R. A. Chipman, S. C. McClain, The Airborne Multiangle SpectroPolarimetric Imager (AirMSPI): A new tool for aerosol and cloud remote sensing, *Atmospheric Measurement Techniques*, vol. 6, no. 8, pp. 2007-2025, 2013.